



Graphitic carbon nitride-carbon nanofiber as oxygen catalyst in anion-exchange membrane water electrolyzer and rechargeable metal–air cells

Ji Eun Park^{a,1}, Mi-Ju Kim^{b,1}, Myung Su Lim^c, Sun Young Kang^c, Jong Kwan Kim^c,
Seung-Hyeon Oh^c, Min Her^{a,b}, Yong-Hun Cho^{c,*}, Yung-Eun Sung^{a,b,**}

^a Center for Nanoparticle Research, Institute for Basic Science (IBS), Seoul, 08826, Republic of Korea

^b School of Chemical and Biological Engineering, Seoul National University, Seoul, 08826, Republic of Korea

^c Department of Chemical Engineering, Kangwon National University, Samcheok, Gangwon-do, 25913, Republic of Korea

ARTICLE INFO

Keywords:

Graphitic carbon nitride
Carbon nanofiber
Anion-exchange membrane water electrolyzer
Zinc–air cell
Bifunctional catalyst

ABSTRACT

Graphitic carbon nitride-carbon nanofiber (g-CN-CNF) was synthesized as a bifunctional catalyst in an anion-exchange membrane water electrolyzer (AEMWE), and primary and rechargeable Zn–air cells. The g-CN-CNF catalyst shows high catalytic activity for oxygen reduction reaction and oxygen evolution reaction in half-cell, with low overpotentials and low Tafel slopes. The high activity is attributed to the synergistic effect of abundant active sites and the electrical conductivity following the pyrolysis of g-CN and CNF. As a result, AEMWE with the g-CN-CNF anode, the first application of a carbon-based catalyst, exhibits outstanding performance that is the highest record in the literature for AEMWE using a non-noble metal catalyst. In addition, the performance and durability of Zn–air cells with g-CN-CNF cathode outperform those fabricated with commercial platinum.

1. Introduction

The development of a low-cost, highly active, and durable catalyst for oxygen electrocatalysis is crucial for the efficient functioning of fuel cells, water electrolyzers, and rechargeable Zn–air cells. It is well established that the oxygen reduction reaction (ORR) plays a key role in determining the performance of fuel cells [1–3]. By contrast, the oxygen evolution reaction (OER) is the core process in water electrolyzers [4,5]. Bifunctional catalysts that are active toward both OER and ORR are of significant importance for the development of rechargeable Zn–air cells [6–8]. The kinetics of oxygen electrocatalysis are sluggish, and thus, platinum and iridium-based noble catalysts that have active toward ORR and OER, respectively, are typically used to increase the efficiency [2,9–11]. However, the high cost of these noble catalysts has been an obstacle in their commercialization. These noble catalysts also have the limitation of catalytic activity and durability. Therefore, it is highly desirable to develop low-cost, active, and durable catalysts based on earth-abundant materials as alternatives.

Graphitic carbon nitride (g-CN) is a material that consists of carbon and nitrogen atoms, organized in a graphite-like framework [12]. Recently, g-CN has been shown to have active as an electrochemical catalyst owing to its high content of N [13–21]. Furthermore, various

approaches to enhancing the catalytic activities of g-CN-based materials as alternatives to noble metals for OER and ORR have been developed [15–18,21]. One such approach involves the addition of a metal to g-CN to improve its catalytic activity. Jiang et al. [18] investigated g-CN-supported single-atom transition metals (Pt, Pd, Co, Ni, Cu) as OER catalysts. Among the transition metals examined, Co exhibited the most outstanding activity. Qiao et al. [21] reported the fabrication of Co-g-CN/carbon nanotube (CNT) materials as electrocatalysts for OER and ORR. Another approach is based on the formation of g-CN/carbon composite nanomaterials to address the drawbacks associated with g-CN. Sun et al. [17] investigated the possibility that a g-CN nanosheets/graphene composite could exhibit OER activity as a result of the presence of pyridinic N active sites. The authors showed that the introduction of graphene into g-CN resulted in a catalyst with good durability and high activity. Qiao et al. [16] reported that a g-CN/CNT three-dimensional porous composite exhibits high OER activity owing to the enhanced mass transport caused by the presence of CNTs. Guo et al. [22] showed that the combination of g-CN with graphene nanosheets produced a metal-free ORR catalyst. Previously, we have synthesized a g-CN/carbon nanofiber (CNF) composite (g-CN-CNF) using a facile preparing method and utilized it in the fabrication of a practical proton-exchange membrane fuel cell (PEMFC) and anion-

* Corresponding author at: Department of Chemical Engineering, Kangwon National University, Samcheok 25913, Republic of Korea.

** Corresponding author at: Center for Nanoparticle Research, Institute for Basic Science (IBS), Seoul 08826, Republic of Korea.

E-mail addresses: yhun00@kangwon.ac.kr (Y.-H. Cho), ysung@snu.ac.kr (Y.-E. Sung).

¹ These authors contributed equally to this work.

exchange membrane fuel cell (AEMFC) [3]. We confirmed that the g-CN-CNF catalyst exhibits high catalytic activity for ORR in alkaline media and high performance in practical fuel cells, demonstrating thus the feasibility of its application in practical electrochemical devices.

Recently, the application of OER or bifunctional catalysts in practical devices such as anion-exchange membrane water electrolyzers (AEMWEs) and rechargeable metal-air cells has been reported, which allows one to evaluate real device performance rather than that of half-cells (determined by the rotating disk electrode (RDE) method). However, for AEMWEs, the application of OER catalysts in full-cell systems has not been extensively investigated. So far, Co- [4], Ni- [5,23], and Cu-based [24,25] materials have been proposed as OER catalysts for AEMWEs. Scott et al. [4] proposed Li-doped Co₃O₄ as an OER catalyst and evaluated its performance in single-cell AEMWEs, achieving a current density of 300 mA cm⁻² at 2.05 V. Similarly, Xing et al. [5] employed core-shell-structured Ni-based hollow spheres for the same purpose, exhibiting a current density of 357.6 mA cm⁻² at 1.8 V. Thus, the application of carbonaceous materials as OER catalysts in AEMWE single cells needs to be further developed.

In addition, various bifunctional catalysts for the oxygen electrode of rechargeable metal-air cells have been reported. Dai et al. [26] investigated N-doped carbon-supported Co materials as catalysts for rechargeable Zn-air cells, achieving performances compared with those of conventional noble metal catalysts. Zhi et al. [27] developed N, S, and O-doped carbon materials as metal-free bifunctional catalysts, showing that they exhibited high catalytic activity and good durability due to the high doping level and hierarchically porous structure. Furthermore, compared to those containing Pt/C as the catalyst, the rechargeable Zn-air cells containing the N, S, and O-doped carbon exhibited a small charge-discharge voltage gap and superior stability.

In the present work, we synthesized a carbonaceous material, g-CN-CNF, as a bifunctional catalyst for oxygen electrocatalysis, and tested its activity toward both ORR and OER in alkaline media. Various synthetic parameters (heat treatment temperature, and content of CNF) were investigated to achieve optimum cell performance. Catalytic activity and durability measurements were conducted using the RDE method. In addition, three types of single cells were prepared to investigate the possibility of g-CN-CNF application in practical electrochemical devices: AEMWE, primary Zn-air cell, and rechargeable Zn-air cell. AEMWE was fabricated and evaluated to examine the practical OER performance. To the best of our knowledge, this work represents the first application of a carbonaceous material as OER catalyst in practical AEMWE. In addition, a primary cell was constructed to examine the ORR activity of g-CN-CNF. Finally, the rechargeable Zn-air cell prepared with g-CN-CNF was evaluated using a long-duration cycling test in order to examine its catalytic activity and stability as a bifunctional catalyst.

2. Experimental

2.1. Fabrication of g-CN-CNF catalyst

The modified preparation procedure employed for the synthesis of g-CN-CNF was based on our previous work [3]. Melamine (1 eq.) was suspended in dimethylformamide (DMF) and subsequently added to *N,N*-diisopropylethylamine (Sigma Aldrich Co., USA). Cyanuric chloride (1 eq.) was added dropwise and the mixture was subsequently stirred for 1 h at 0 °C. The temperature was increased to room temperature and the solution was stirred for additional 18 h. An additional quantity of cyanuric chloride (1 eq.) was added dropwise and the solution was stirred for 1 h at 0 °C. Subsequently, the temperature was increased to room temperature and the solution was stirred for 7 h. In order to increase the conductivity of the catalyst, the CNF (Carbon Nanomaterial Technology Co., Korea) was added dropwise to the solution. The mass ratio of CNF was approximately 30, 50, and 70 wt. % relative to total mass to examine the optimal content of CNF in g-CN-

CNF. To remove any trace metal residues on the surface, the CNF was treated with acid (4 M H₂SO₄:4 M HNO₃, 3:1, v:v) for 7 h at 90 °C before its addition to the solution. The mixture was refluxed for 24 h at 150 °C under argon atmosphere. The precipitate was filtered and washed with ethanol. The prepared catalyst was dried using oven at 105 °C. For pyrolysis, the synthesized g-CN-CNF was heated to a certain temperature under an argon atmosphere for 7 h and maintained at the target level for 30 min. Three temperatures (700, 800, and 900 °C) were examined in order to determine the optimal temperature.

2.2. Electrochemical characterization of g-CN-CNF

The half-cell experiments were performed with an Autolab potentiostat in the form of a three-electrode cell at 25 °C. We used glassy carbon electrode and saturated Ag/AgCl as the counter and the reference electrode, respectively. For the fabrication of the ink, 5 mg of the catalysts were mixed and sonicated with 30 μ L of 5 wt. % Nafion ionomer and 700 μ L of isopropanol. We loaded 20 μ L of the ink onto a glassy carbon electrode. As standard materials, 20 wt. % Pt/C (Johnson Matthey Co. UK) and IrO₂ (Alfa Aesar Co., USA) were used. The densities of the loaded ink were 800 μ g/cm² for g-CN-CNF materials and 400 μ g/cm² for standard materials. The hydrogen oxidation reaction was performed to convert the measured potential to a reversible hydrogen electrode (RHE). During linear sweep voltammetry (LSV) for ORR and OER, the rotating disk electrode (RDE) was scanned at a rate of 10 mV/s in an O₂-saturated 0.1-M KOH solution at a rotating speed of 1600 rpm. ORR and OER LSV curves were iR-corrected, and the ORR curves were corrected with LSV curves measured in Ar-saturated electrolyte. The rotating ring-disk electrode (RRDE, Pine research) analysis was conducted in an O₂-saturated 0.1-M KOH solution at a scan rate of 10 mV/s and a rotating speed of 1600 rpm. A collection efficiency of 0.37 and a ring voltage of 1.2 V versus RHE were used to obtain electron transfer numbers and peroxide yields. Chronoamperometry was conducted using a voltage of 0.7 V versus RHE, and 3 mL of methanol were added after 100 s to confirm the methanol tolerance of the catalysts. Durability tests for ORR and OER operating conditions were chronoamperometrically performed in O₂-saturated electrolyte at a rotation speed of 1600 rpm at voltages of 0.7 and 1.6 V vs. RHE, respectively.

2.3. AEMWE and Zn-air cell test

In order to examine the OER activity of the synthesized catalyst, the AEMWE performance was evaluated. The single cell consists of a membrane-electrode assembly (MEA), gas diffusion layer (GDL), and bipolar plates. The MEA was fabricated using the catalyst-coated membrane (CCM) method with an active area of 5 cm². In the present work, Fumapem FAA-3-50 (FuMA-Tech Inc., Germany) was used as the anion-exchange membrane, and 40 wt. % Pt/C (Johnson Matthey Co. UK) with a loading of 0.4 mg-cm⁻² was used as the HER catalyst. The g-CN-CNF-800 and commercial IrO₂ (Alfa Aesar Co., USA) were used as the OER catalyst. The cell temperature was set to 60 °C, and 1.0 M KOH solution was fed into the anode and cathode at a rate of 1 mL·min⁻¹ [28]. Prior to operation, 1.0 M KOH solution was allowed to flow for 10 min to supply reactants to the entire catalyst layer. The cell voltage was applied from 1.35 V to 2.15 V with an interval of 0.05 V to evaluate the cell performance. The electrochemical impedance spectroscopy (EIS, ZAHNER-elektrik GmbH & Co. KG, Germany) analysis was performed at a constant voltage of 1.9 V to characterize the ohmic and charge transfer resistances. The frequency ranged from 100 mHz to 100 kHz during this measurement.

To characterize the ORR activity of g-CN-CNF, a homemade primary cell was prepared with an active area of 5 cm² (Supplementary note and Fig. S1). The catalyst loadings of g-CN-CNF-800 and 40 wt. % Pt/C were both 4.0 mg-cm⁻². The cell temperature was maintained at 25 °C. Two tests were carried out: (i) current sweep method and (ii) constant

current method. Using the current sweep method, polarization curves were obtained to evaluate the performance of a Zn–air cell with g-CN–CNF-800. In addition, the specific density and energy density were measured using the constant current method at $10 \text{ mA}\cdot\text{cm}^{-2}$. The EIS data were obtained at a constant voltage of 1.1 V to characterize the ohmic and charge transfer resistances of two catalysts. The frequency ranged from 100 mHz to 100 kHz during these measurements.

The rechargeable cell was constructed to evaluate the bifunctional activity of g-CN–CNF for ORR and OER. Two types of cycling tests were performed to evaluate the stability of g-CN–CNF as a bifunctional catalyst [29]. The first test is the pulse cycling test, which involves a large number of short-duration cycles (200 s). This method can examine the stability of an air electrode. The second method consists of a small number of long-duration cycles (30 min). This method can evaluate the real retention of the Zn–air cell. The performance was measured at a constant current density of $10 \text{ mA}\cdot\text{cm}^{-2}$. By using these two methods, the catalytic stability of g-CN–CNF-800 was investigated.

3. Results and discussion

3.1. Characterization of the synthesized g-CN–CNFs

The synthetic procedure for the preparation of the g-CN–CNF catalyst involved three main steps (Fig. 1): (i) the fabrication of g-CN using cyanuric chloride and melamine via a stepwise synthesis, (ii) the addition of CNFs, which were treated with acid, to g-CN to increase the catalyst conductivity, (iii) heat treatment (HT) of the resulting g-CN–CNF at 700, 800, or 900 °C under Ar atmosphere for pyrolysis. This process afforded different g-CN–CNF materials that allowed the optimal HT temperature to be determined. The g-CN–CNFs subjected to different HT temperatures are referred to as g-CN–CNF-T, where T presents the temperature (noHT, 700, 800, and 900 °C). Additionally, several g-CN–CNFs were prepared with different wt. % of CNFs (30, 50, and 70 wt. %) at the optimal HT temperature of 800 °C. The prepared catalysts are referred to as g-CN–CNF-Nwt, where N represents the wt. % content of CNFs (30, 50, and 70 wt. %).

As shown in the SEM image of g-CN (Fig. S2 (a,b)), the synthesized g-CN particles were agglomerated. The specific surface area of g-CN was determined to be $66.69 \text{ m}^2\cdot\text{g}^{-1}$ using the Brunauer–Emmett–Teller (BET) method (Fig. S3 (a)). In addition, the average pore diameter was calculated to be approximately 8.7 nm via Barrett–Joyner–Halenda (BJH) adsorption (Fig. S3 (b)). Fig. S2 (c) shows the Fourier transform infrared (FT-IR) spectrum of the synthesized g-CN. Comparison of the FTIR spectrum obtained for the synthesized g-CN material with literature reports revealed a good agreement [30–32]. The peaks observed at about 806, 1200–1605, and 3000–3500 cm^{-1} are associated with the triazine ring mode, the stretching modes of CN heterocycles, and stretching modes of amines, respectively [32]. In addition, the XRD pattern of g-CN synthesized here matches the typical pattern expected for g-CN, with peaks at approximately 11.1° and 27.4° (Fig. 2(a)) [3,33]. The peak at $\sim 11.1^\circ$ is ascribed to the in-plane structural

packing of triazine, while the peak at 27.4° is associated with the interlayer stacking of aromatic rings. The TGA curve (Fig. S2 (d)) measured under N_2 atmosphere showed that g-CN was fully decomposed at temperatures above 800 °C; this result is in agreement with the reported characteristics of g-CN [13].

The SEM images (Fig. 3(a,b)) showed that the g-CN–CNF-800 was combined with g-CN and CNF. When compared to the g-CN particles shown in Fig. S2 (a,b), the g-CN nanoparticles in the g-CN–CNF-800 material were uniformly dispersed with CNF, indicating the successful deposition of g-CN on CNF. As displayed in Fig. 3 (c), TEM also showed that the CNFs were surrounded by g-CN particles. EDS mapping (Fig. 3(d–g)) confirmed the homogeneous distributions of C, N, and O atoms in g-CN–CNF-800, indicating that N atoms were uniformly dispersed in g-CN–CNF. The BET surface area of g-CN–CNF-800 ($171.63 \text{ m}^2\cdot\text{g}^{-1}$) was considerably higher than that of g-CN ($66.69 \text{ m}^2\cdot\text{g}^{-1}$). Further, the N adsorption isotherm of g-CN–CNF-800 exhibited a rapid increase in high relative pressure ($P/P_0 > 0.9$), suggesting the presence of secondary pores [34] (Fig. S3 (a)). Moreover, the pore volume between 1.7 nm and 300 nm, and average pore diameter were determined using the BJH method to be $0.43 \text{ cm}^3\cdot\text{g}^{-1}$ and 17 nm, respectively (Fig. S3 (b)).

Fig. 2(a) shows the X-ray diffraction (XRD) patterns of the synthesized g-CN–CNF-T materials. These patterns show that as the HT temperature was increased from 700 to 900 °C, the peak intensity increased, indicating increased degree of graphitization. In addition, all the materials exhibited XRD patterns that were more similar to that of CNF, rather than the XRD pattern of g-CN. As shown in Fig. 2(b), the Raman spectra of all samples exhibited two distinct peaks at approximately 1345 and 1580 cm^{-1} . The D band observed at 1345 cm^{-1} is associated with disordered carbon, whereas the G band at 1580 cm^{-1} is related to the graphitization [35]. In addition to the XRD patterns, the Raman spectra showed that the I_D/I_G ratio of the g-CN–CNF-T materials decreased as the HT temperature was increased, leading to increased degree of graphitization.

X-ray photoelectron spectroscopy (XPS) was used to investigate the surface composition of each g-CN–CNF-T. The XPS survey spectra reveal the presence of C, N, and O (Fig. S4). While g-CN–CNF-noHT exhibited four peaks for C–C (284.6 eV), C–O/C–N (285.7 eV), C=O/C=N (287.9 eV), and O–C=O (288.91 eV) species [36,37], other g-CN–CNF-T materials subjected to HT showed three distinct peaks, i.e., the peak arising from O–C=O species was missing (Fig. S5)). In addition, the intensity of the peak associated with C–C species of g-CN–CNF-T increased as the HT temperature increased. These changes can be attributed to the decrease in the content of O atoms after pyrolysis. Furthermore, the presence of the peaks related to the C–O/C–N and C=O/C=N species indicates that the N atoms from g-CN, which could serve as active sites for oxygen electrocatalysis, were successfully doped into CNF. Fig. 2(c–f) shows the XPS spectra of N 1s of g-CN–CNF-Ts. The deconvolution of the peaks observed revealed four types of N configurations—pyridinic (398.6 eV), pyrrolic (399.89 eV), graphitic (401.1 eV), and oxidized N (402.6 eV). Unlike g-CN–CNF-noHT, which

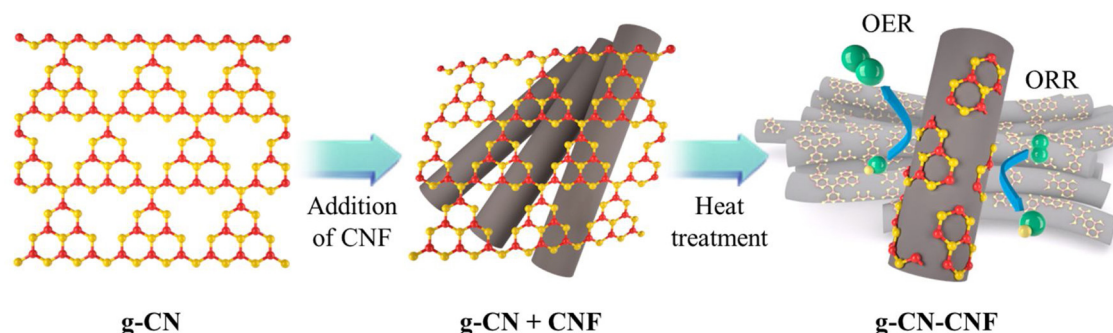


Fig. 1. (a) Schematic diagram showing the preparation of the g-CN–CNF catalyst.

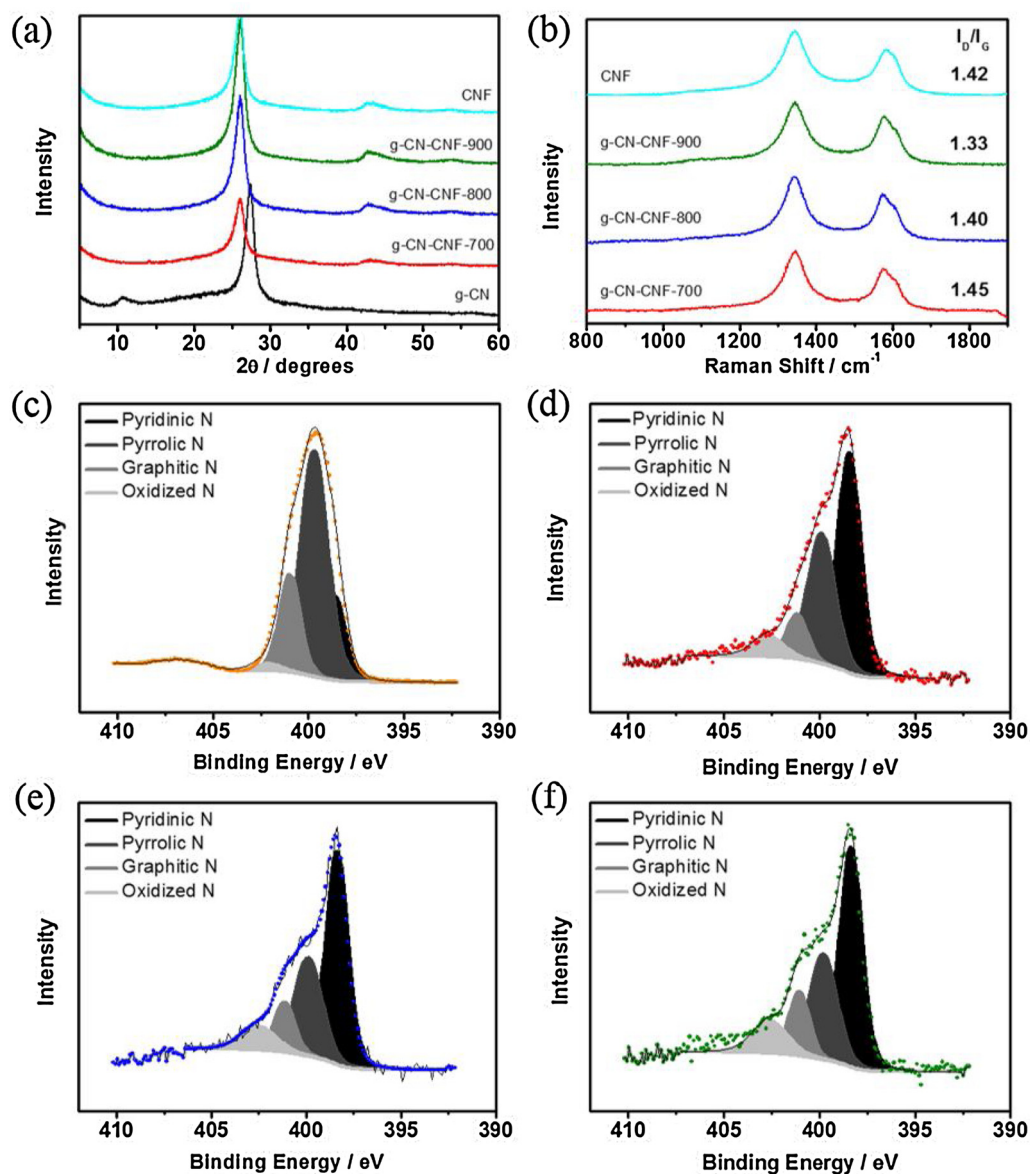


Fig. 2. (a) XRD patterns of g-CN, g-CN-CNF-T and CNF materials. (b) Raman spectra of g-CN-CNF-T and CNF materials. N 1s XPS spectra of (c) g-CN-CNF-noHT, (d) g-CN-CNF-700, (e) g-CN-CNF-800, and (f) g-CN-CNF-900.

was mainly comprised of pyrrolic N, the other g-CN-CNF-T materials contained high contents of pyridinic N (Table S1). The atomic percentages of pyridinic N in the g-CN-CNF-T materials (noHT, 700, 800, and 900 °C) were 17.30, 49.79, 50.64, and 47.77%, respectively. The percentages of graphitic N for the same four g-CN-CNF-Ts were 17.30, 9.18, 11.28, and 12.85%, respectively. Among the g-CN-CNF-Ts examined, g-CN-CNF-800 displayed the largest percentage of nitrogen atoms in pyridinic and graphitic configurations (61.92%), which are known to be active sites for oxygen electrocatalysis [38–40]. It is expected therefore that the increased levels of pyridinic and graphitic N will manifest in enhanced catalytic activity. In addition, the N contents of the g-CN-CNF-T materials were confirmed by elemental analysis (Table S1). The N contents of g-CN-CNF-noHT, g-CN-CNF-700, g-CN-CNF-800, and g-CN-CNF-900 were 21.74, 3.15, 2.53, and 2.56 wt. %, respectively. The N contents of g-CN-CNF-700, -800, and -900 (2–3 wt. %) were much lower than that of g-CN-CNF-noHT (21.74 wt. %), indicating that a significant proportion of N atoms was lost during the high temperature pyrolysis.

The series of g-CN-CNF-Nwt materials (CNFs: 30, 50, and 70 wt. % of total mass) were characterized to examine the effect of the wt. %

contents of g-CN and CNF (Fig. S6 and S7). All the g-CN-CNF-T materials, which were discussed earlier on, were prepared using g-CN = 50 wt. % and CNF = 50 wt. %. To determine the optimal CNF content in g-CN-CNF, the g-CN-CNF-Nwt materials were synthesized at the optimal HT temperature of 800 °C. Table S2 summarizes the N contents, properties, and binding energies of the various g-CN-CNF-Nwt materials prepared. While the sum of the atomic percentage contents of pyridinic N and graphitic N increased as the wt. % of CNF (55.33, 61.92, and 64.21 at. %) increased, the total N content was the largest for the g-CN-CNF-50 wt sample. The differences in the N contents of the g-CN-CNF-Nwt materials are ascribed to the changes in the quantities of g-CN and CNF employing during the preparation of the samples. During pyrolysis, the decomposed g-CN was deposited on CNFs, serving thus as the N source in CNFs. When the wt. % content of g-CN was lower than that of CNF, the small amount of g-CN deposited resulted in reduced N content. By contrast, when the wt. % content of g-CN was higher than that of CNF, the insufficient amount of CNFs, which act as the substrate, resulted in the reduced overall N content in the sample. As a consequence, the sample prepared at 50 wt. % of both g-CN and CNFs was determined to be optimal for achieving high N content. The g-

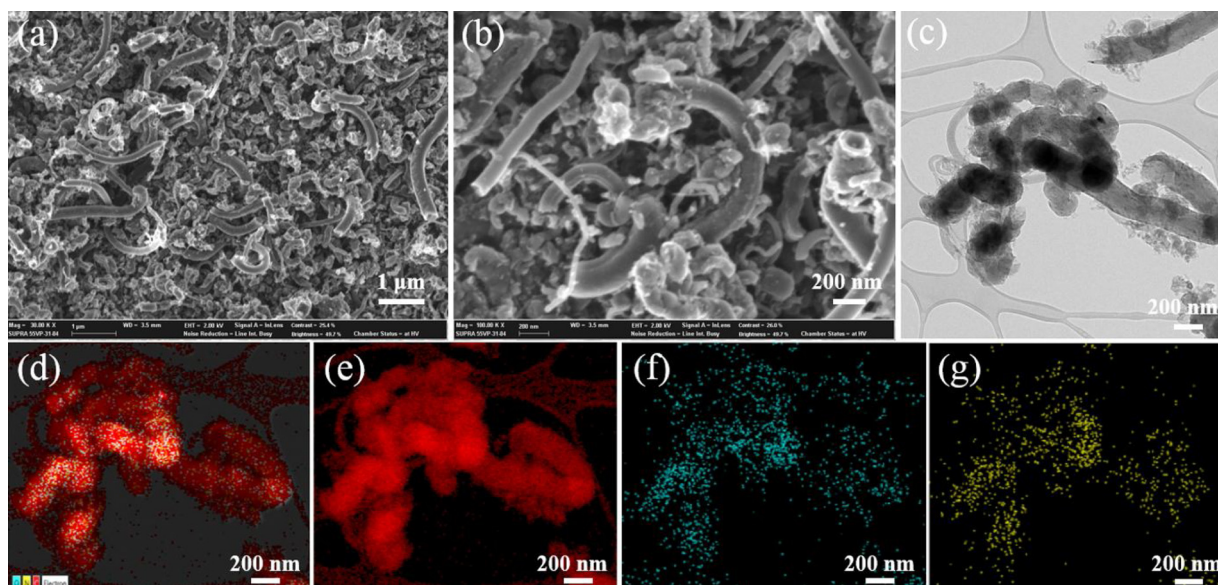


Fig. 3. (a,b) SEM images, (c) TEM image, and (d–g) EDX elemental mapping of g-CN-CNF-800 electrocatalyst.

CN-CNF-50 wt material has the highest contents of pyridinic and graphitic Ns of all the catalysts examined, and is thus expected to exhibit the highest catalytic activity. As shown in Fig. S8 (a), the BET surface areas of g-CN-CNF-30 wt, g-CN-CNF-50 wt, and g-CN-CNF-70 wt were 179.5, 171.6, and 156.56 m^2g^{-1} , respectively, indicating that the specific surface area decreased with increasing content of CNFs. By contrast, the pore volumes for these samples were determined to be 0.349, 0.433, and 0.354 cm^3g^{-1} . Taken together, the optimal content of CNFs is confirmed to be 50 wt. % based on the high N content and pore volume.

3.2. Electrochemical characterization of the synthesized g-CN-CNFs

The results of the electrochemical analyses using a half-cell configuration are summarized in Fig. 4. The ORR LSV curves of g-CN-CNF-

T materials were measured with RDE in a 0.1-M KOH electrolyte (Fig. 4(a)). CNF, i.e., the carbon support, exhibits relatively poor performance with non-flat and small limiting currents, which imply that CNF has a low electron transfer number. The improved performance of g-CN-CNF-T materials indicates the synergistic impact of the combination of g-CN and CNFs following pyrolysis [15]. Among the g-CN-CNF-T materials examined, g-CN-CNF-800 exhibited the greatest catalytic performance in terms of half-wave potential (0.814 V), onset potential (0.943 V at $-0.1 \text{ mA}\cdot\text{cm}^{-2}$) and limiting currents ($-5.57 \text{ mA}\cdot\text{cm}^{-2}$). Interestingly, g-CN-CNF-700 (0.941 V) displayed a larger limiting current ($-5.29 \text{ mA}\cdot\text{cm}^{-2}$) than g-CN-CNF-900 despite its onset potential being similar to that of g-CN-CNF-900 (0.900 V). The superior catalytic activity of g-CN-CNF-800 was also confirmed by the results of the RRDE analysis (Fig. 4(b)) and the Koutecky–Levich method (Fig. 4(c) and Fig. S9). While the peroxide produced during the

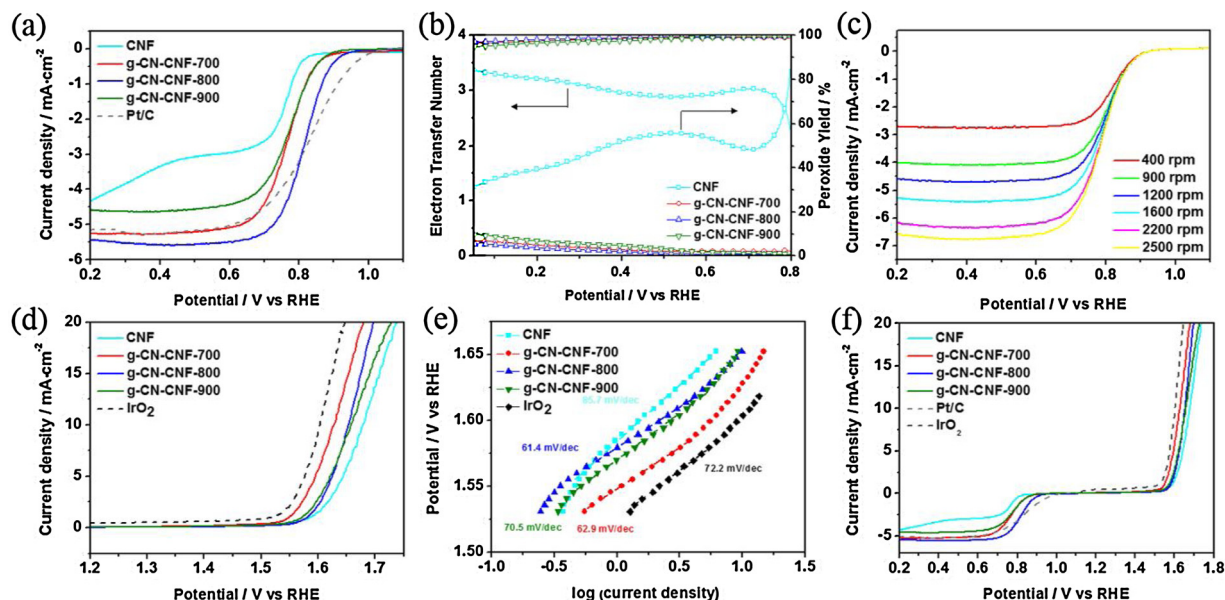


Fig. 4. (a) Linear sweep voltammogram curves of g-CN-CNF-T materials for ORR at a scanning rate of 10 mV/s with iR correction. (b) Electron transfer numbers and peroxide yields of g-CN-CNF-T materials derived from RRDE analysis. (c) Linear sweep voltammogram curves of g-CN-CNF-800 at different rotating speeds. (d) Linear sweep voltammogram curves of g-CN-CNF-T materials for OER at a scanning rate of 10 mV/s with iR correction. (e) Tafel plots derived from (d). (f) Oxygen catalytic activities of g-CN-CNF-T materials.

application of voltage exceeds 60% in the case of CNF, g-CN-CNF-T materials produced less than 10% of peroxide, and the corresponding electron numbers were close to 4.0. The g-CN-CNF-800 catalyst exhibits the lowest peroxide yield and the highest electron transfer number. The electron transfer number of g-CN-CNF-800, calculated based on Koutecky–Levich plots, was 3.81 at 0.2 V.

Fig. 4(d) shows the OER LSV curves of g-CN-CNF-T materials after iR compensation. As observed for the ORR performances, the g-CN-CNF-T materials exhibited improved OER activities when compared to that of CNF. The g-CN-CNF-700 displayed the best performance with an overpotential of 398 mV at $10 \text{ mA}\cdot\text{cm}^{-2}$, followed by an overpotential of 422 mV for g-CN-CNF-800 and 427 mV for g-CN-CNF-900. The Tafel plots shown in Fig. 4(d) were collected to investigate the OER mechanisms of the samples. The g-CN-CNF-800 showed the lowest Tafel slope of $61 \text{ mV}\cdot\text{dec}^{-1}$, even lower than that of IrO_2 ($72.2 \text{ mV}\cdot\text{dec}^{-1}$), which indicates the effectiveness of g-CN-CNF-800 [41]. To confirm the applicability of the prepared materials as bifunctional oxygen catalysts, the variances in the ORR and OER parameters derived from the LSV curves were compared (Fig. 4(f) and Fig. S9). The ΔE value of the catalysts, which represents the difference between the half-wave potential of ORR LSV curves and the potential at $10 \text{ mA}\cdot\text{cm}^{-2}$, determines the effectiveness of both ORR and OER, and thus also the efficiency of the rechargeable reactions. The g-CN-CNF-700 (0.863 V) and g-CN-CNF-900 (0.885 V) exhibited enhanced oxygen catalysis when compared to CNF (0.916 V). The lowest value of ΔE was obtained for g-CN-CNF-800 (0.863 V), and is indicative of favorable bifunctional catalytic reactions. The excellent catalytic performance of g-CN-CNF-800 is the result of adequate degree of graphitization and the presence of sufficient active sites, derived from abundant graphitic N and pyridinic N [42]. In detail, graphitic N transfers electrons to the surrounding carbon, increasing thus the adsorption of oxygen and eventually increasing ORR performance. In addition, pyridinic N can attract electrons from the surrounding carbon, thereby helping to adsorb hydroxyl ions and increasing OER performance [7]. Methanol tolerance and long-term durability tests were conducted to evaluate the catalytic abilities of g-CN-CNF-800 as the alternative to platinum-based catalysts. The results showed that ORR activity of g-CN-CNF-800 maintains the current after the addition of methanol (Fig. S10 (a)), and displays stable current even after 45,000 s; this performance is better than those of commercial platinum catalysts (Fig. S10 (b)). Moreover, Fig. S11 shows that the OER activity of g-CN-CNF-800 exhibited good durability for 45,000 s, surpassing that of commercial IrO_2 despite the occurrence of carbon corrosion caused by high anodic potentials, as has been reported for other CNF-based catalysts [43].

The catalytic activities of g-CN-CNF-Nwt materials were also investigated to ascertain the optimum ratio of g-CN and CNF. The analysis revealed that the lower g-CN content of g-CN-CNF-30 wt led to an uneven limiting current in the ORR LSV curve (Fig. S12 (a)). By contrast, the g-CN-CNF-70 wt catalyst containing high g-CN content exhibited lower half-wave potential than g-CN-CNF-50 wt, despite the fact that the values of their limiting current were similar. This result can be ascribed to the small content of nitrogen in this sample (Table. S4). In terms of the OER performances (Fig. S12 (b)), although the onset potential of g-CN-CNF-70 wt was lower than those of the other samples, g-CN-CNF-50 wt displayed better activity at high current density owing to its small Tafel slope (Fig. S12 (c)). Based on the ΔE values shown in Table S4 and Fig. S12 (d), the increase in the g-CN content of the g-CN-CNF-Nwt generally enhanced the oxygen catalytic activity of the material. The lowest ΔE value was observed for g-CN-CNF-50 wt (0.838 V), and can be attributed to its high nitrogen content, especially in the graphitic and pyridinic nitrogen configurations.

3.3. AEMWE performance

As illustrated in Fig. 5(a), an AEMWE with g-CN-CNF-800 as the anode and Pt/C as the cathode was fabricated to evaluate its OER

activity for practical use. Fig. 5 (b) shows the changes in the cell performance of AEMWE as a function of the catalyst loading (2, 4, 6, and $8 \text{ mg}\cdot\text{cm}^{-2}$). As the catalyst loading was increased from 2 to 4, and subsequently to $6 \text{ mg}\cdot\text{cm}^{-2}$, the cell performance improved as a result of the increased number of active sites (223, 350, and $734 \text{ mA}\cdot\text{cm}^{-2}$, respectively). However, the cell performance at the highest catalyst loading ($8 \text{ mg}\cdot\text{cm}^{-2}$) decreased from $734 \text{ mA}\cdot\text{cm}^{-2}$ to $487 \text{ mA}\cdot\text{cm}^{-2}$ as a result of the thicker catalyst layer. Therefore, AEMWE exhibited the best performance, i.e., a current density of $734 \text{ mA}\cdot\text{cm}^{-2}$ at 1.9 V, when the catalyst loading was $6 \text{ mg}\cdot\text{cm}^{-2}$. Furthermore, g-CN-CNF-800 exhibited an outstanding performance when compared to commercial IrO_2 despite the fact that it is based on a carbonaceous material, and not a noble metal (Fig. 5(c)). The current density of g-CN-CNF-800 at 1.9 V was 53% higher than that of IrO_2 . Additionally, EIS was used to investigate the resistances in AEMWE [44]. As shown in Fig. S13, the g-CN-CNF-800 showed similar ohmic resistance, and smaller charge transfer resistance when compared to IrO_2 . Although the g-CN-CNF-800 was thicker ($40 \mu\text{m}$) than IrO_2 ($2 \mu\text{m}$), its high conductivity resulted in similar ohmic resistance. In addition, as shown in Fig. S14, the fraction of secondary pores in the g-CN-CNF catalyst layer exceeded that observed for IrO_2 . The higher portion of the secondary pores in the g-CN-CNF catalyst layer resulted in improved interfacial reaction kinetics and mass transport, leading thus to a smaller charge transfer resistance despite the lower catalytic activity mentioned in Section 3.2 and shown in Fig. S15. Fig. 5(d) compares the cell performances of several non-noble catalysts reported in the literature (full symbols) [4,5,23–25,45] with the performance of the carbonaceous catalysts synthesized in this work (open symbols). To the best of our knowledge, this comparison suggests that g-CN-CNF-800 exhibits the highest performance for AEMWE reported to date. Furthermore, no studies have examined the possibility of applying carbonaceous materials as OER catalysts in practical AEMWEs. The results obtained here demonstrated that g-CN-CNF-800 displays notable potential as a catalyst for OER in practical AEMWE.

3.4. Zn–air cell test

In addition to examining the OER activity, we prepared a primary Zn–air cell in order to examine the ORR activity of g-CN-CNF-800 (Fig. S1). Fig. 6(a) shows the cell performance of the primary Zn–air cell utilizing g-CN-CNF-800. The catalyst loadings of g-CN-CNF-800 and 40 wt. % Pt/C in these experiments were both $4.0 \text{ mg}\cdot\text{cm}^{-2}$. The power density of the primary cell incorporating g-CN-CNF-800 was determined to be $160 \text{ mW}\cdot\text{cm}^{-2}$. Although the catalyst loading of g-CN-CNF-800 was identical to that of the 40 wt. % Pt/C, the primary cell utilizing g-CN-CNF-800 exhibited a power density that was approximately 89% of that determined for the 40 wt. % Pt/C. In addition, the specific capacity and energy density of g-CN-CNF-800 were calculated from the time when the cut-off voltage was reached and from the weight of the Zn consumed. The specific capacity and energy density of g-CN-CNF-800 were $363 \text{ mA}\cdot\text{h}\cdot\text{g}^{-1}$ and $388 \text{ mW}\cdot\text{h}\cdot\text{g}^{-1}$, respectively, and were higher than those determined for the 40 wt. % Pt/C (Fig. 6(c,d)). In order to examine the resistance of the primary cell, EIS spectra were obtained at 1.1 V (Fig. S16). The Nyquist plot revealed the presence of two combined arcs, which correspond to the charge transfer resistances of the two electrodes. The low-frequency arc is associated with the charge transfer resistance of the air electrode. As shown in Fig S16, the charge transfer resistance of g-CN-CNF-800 was larger than that of Pt/C. This finding is consistent with the results of the half-cell test. The cell performance of the primary Zn–air cell was comparable to that of the commercial Pt/C. This result is ascribed to the porous catalyst layer formed during the preparation of the air electrode. When the catalyst layer employing the g-CN-CNF-800 catalyst was fabricated onto the GDL, secondary pores were formed as a result of the presence of CNFs (Fig. S17), leading to enhanced mass transport. Overall, therefore, g-CN-CNF-800 exhibited as a result of its structure practical performance

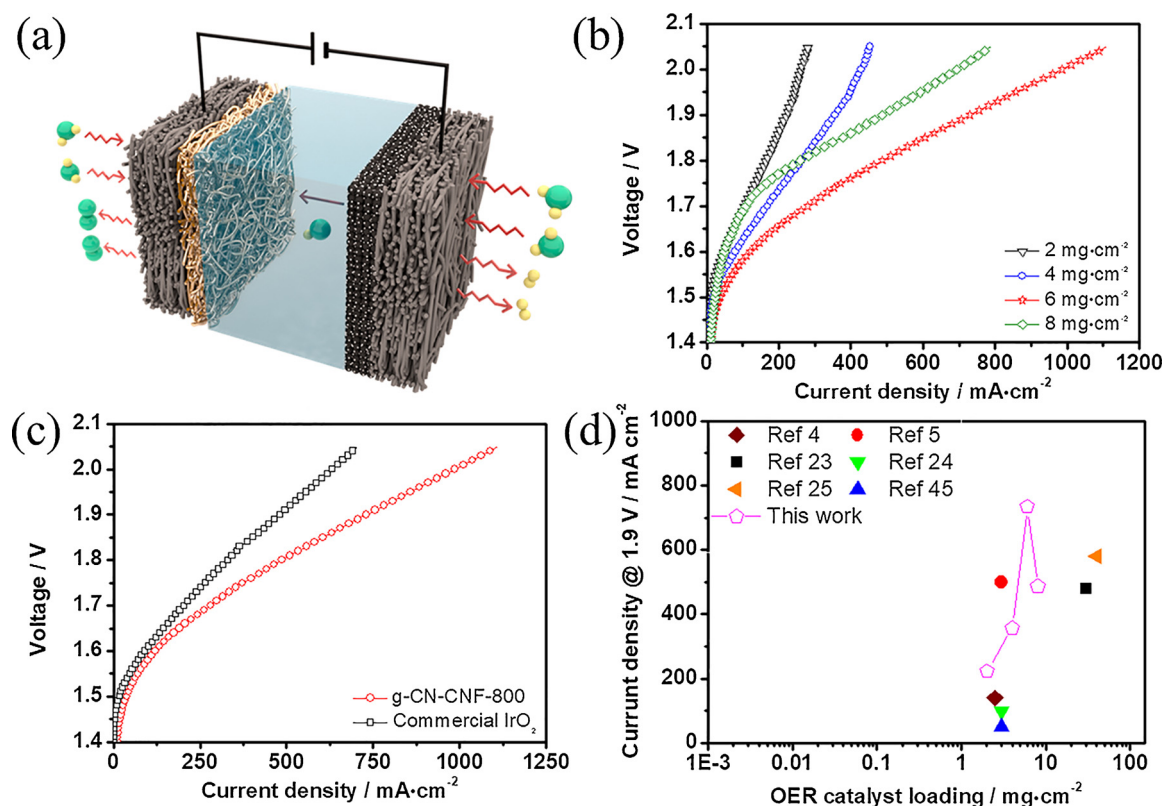


Fig. 5. (a) Schematic diagram of AEMWE single cell with g-CN-CNF-800 as the anode catalyst. (b) Polarization curves obtained for AEMWE with different anode catalyst loadings. (c) Cell performance of AEMWE with g-CN-CNF-800 and commercial IrO₂. (d) The comparison of cell performances (current densities at 1.9 V) reported in literature and in this work (full symbols: non-noble metals as OER catalysts, open symbols: carbon-based material as OER catalyst).

that is comparable to that of a commercial Pt/C.

In order to investigate the capacity of g-CN-CNF-800 to serve as a bifunctional catalyst, a rechargeable cell utilizing this catalyst as the air electrode was constructed (Fig. 7(a)). During the operating conditions (discharge and charge) of the rechargeable cell, both ORR and OER occurred on the g-CN-CNF-800. Fig. 7(b), Fig. S18, and Table S2 represent the long-time cycling performance of g-CN-CNF-800 and Pt/C with short discharge/charge time length (400 s per cycle) at a constant current density of 10 mA·cm⁻². In the first discharge cycle, the discharge potential of Pt/C was 1.33 V; this value is higher than that measured for g-CN-CNF-800. This result is consistent with the ORR activity determined using the half-cell test. However, the charge potential of Pt/C was much larger than that of g-CN-CNF-800 as a result of its lower OER activity. In addition, the gap in discharge potential increased sharply after the 22nd cycle, indicating that Pt/C is not suitable as a bifunctional catalyst for oxygen electrocatalysis. For g-CN-CNF-800, the charge and discharge potentials were 2.01 and 1.18 V, and the rechargeable cell employing g-CN-CNF-800 exhibited good performance, with a round-trip efficiency of 58.7% (Table S5). Furthermore, g-CN-CNF-800 showed good retention of potential gap, with a negligible decrease over 180 cycles. When the long-term operation was examined, the charge potential was maintained at 2.00 V. In this case, the discharge potential decreased by only 3.4%, and the round-trip efficiency changed only by 1.7%.

The rechargeable cell was also examined using a longer time length (1 h per cycle) to examine the real capacity retention of the Zn-air cell. As shown in Fig. 7(c) and Fig. S18, the difference between the discharge and charge potential was smaller than that for Pt/C. Although the cycling test with a time length of 1 h per cycle involved harsh operation conditions, g-CN-CNF-800 exhibited good retention of capacity for 23 h, with no significant change in potential. In addition, the changes in discharge potential and round-trip efficiency were 0.07 V and 3.2%,

respectively (Table S6). Furthermore, the charge potential was maintained at 1.98 V without negligible loss, which was consistent with the durability of OER activity in the RDE test. Although the use of high anodic potentials can induce carbon corrosion and thus decrease durability, g-CN-CNF-800 exhibited good durability in both RDE and practical device tests. Unfortunately, the durability test could not be performed for longer than 23 h as a result of the consumption of the Zn plate. Increase in durability can be expected if a thicker Zn plate (> 250 μm) was used as anode. Overall, the synthesized g-CN-CNF-800 displayed remarkable oxygen catalytic activity and stability. Therefore, the present results indicate that g-CN-CNF-800 is a promising carbonaceous material candidate for a bifunctional catalyst for practical AEMWE and Zn-air cell.

Overall, g-CN-CNF exhibited excellent performance as a metal-free catalyst for both Zn-air cells and AEMWEs (Fig. 5d), featuring half-cell and Zn-air-cell performances similar to those of the recently reported metal-free catalysts (Table S7). The above superior catalytic ability was ascribed to (i) the high electrical conductivity and corrosion resistance of CNF, (ii) the adequate degree of graphitization and sufficient number of active sites, and (iii) the formation of secondary pores. Moreover, g-CN-CNF could be easily prepared on a gram-scale owing to the facile and sustainable nature of the synthetic process (Fig. S19) and was therefore concluded to be suitable for large-scale application in Zn-air cells and AEMWEs.

4. Conclusions

In this work, we successfully synthesized g-CN-CNF and tested its applicability as a bifunctional catalyst for oxygen electrocatalysis in AEMWE and rechargeable Zn-air cell. The g-CN-CNF catalyst showed catalytic activity toward both ORR and OER as a result of the synergistic effect of g-CN and CNF. The catalytic activity is ascribed to the

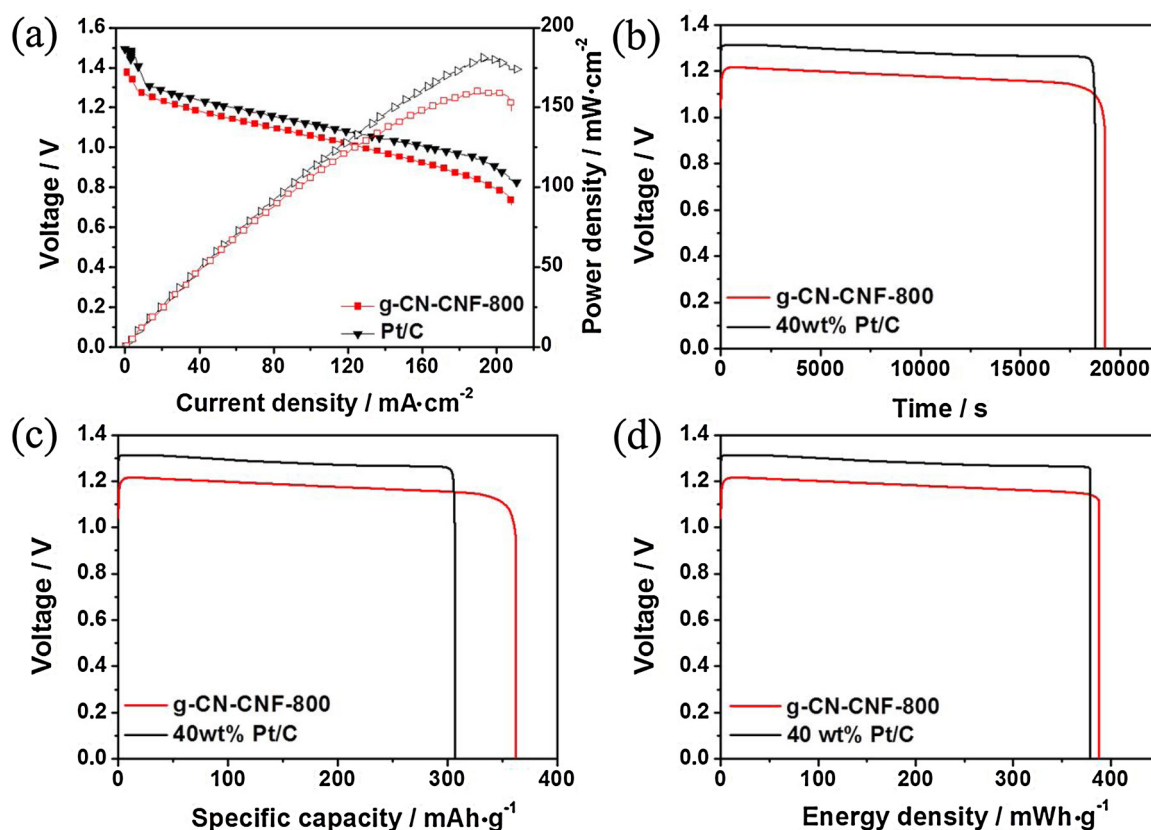


Fig. 6. (a) Polarization curves of g-CN-CNF-800 and Pt/C. (b) Long-time discharge curves of g-CN-CNF-800 and 40 wt. % Pt/C at a constant current density of 10 mA/cm^2 , (c) Typical discharge curves of primary cells with g-CN-CNF-800 and 40 wt. % Pt/C at a constant current density of 10 mA/cm^2 . (d) Energy density plots of g-CN-CNF-800 and 40 wt. % Pt/C at 10 mA/cm^2 .

formation of active sites by the decomposition of g-CN and the enhanced electrical conductivity of the substrate following the pyrolysis. We applied the synthesized g-CN-CNF catalyst to various electrochemical devices in order to examine their practical performance. Examination of AEMWE revealed high performance of $734 \text{ mA}\cdot\text{cm}^{-2}$ at 1.9 V, and represents the first application of a carbonaceous catalyst to practical AEMWE and the best performance reported to date. In addition, the g-CN-CNF showed primary cell performance that was comparable with that of platinum, despite the same catalyst loading.

Furthermore, the cycling test of a rechargeable Zn–air cell revealed that g-CN-CNF exhibits a negligible loss in the charge/discharge potential after 156 cycles, confirming the catalytic activity and stability of g-CN-CNF as a bifunctional catalyst. Therefore, g-CN-CNF is a suitable candidate for the preparation of carbonaceous bifunctional catalysts that can be applied in practical electrochemical devices.

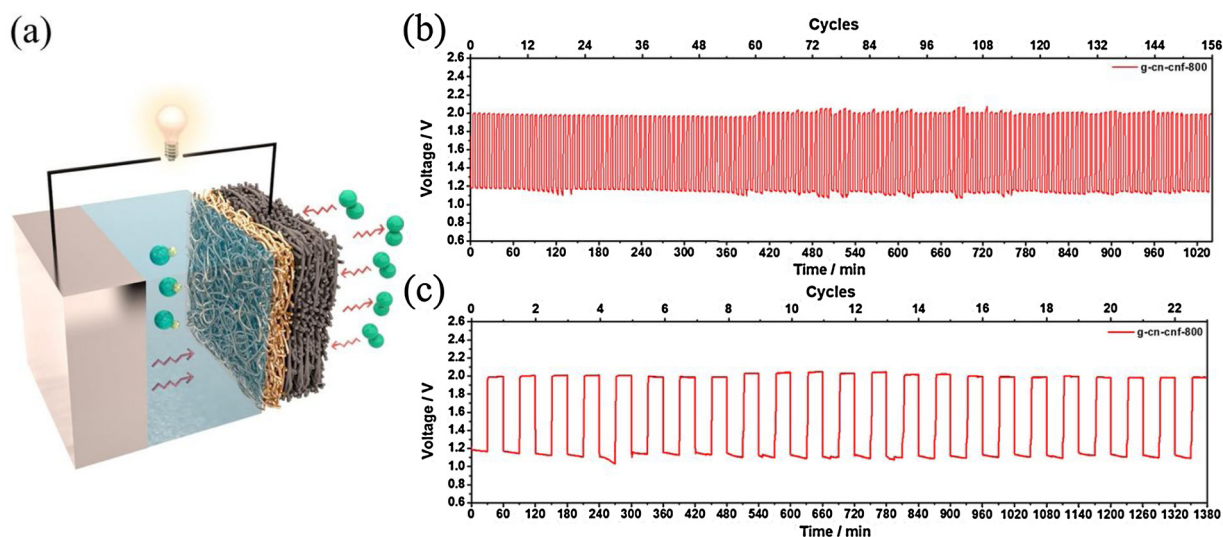


Fig. 7. (a) Schematic diagram of rechargeable Zn–air cell. (b) Long-term cycling performance of g-CN-CNF-800 using short discharge/charge time length (200 s/200 s). (c) Long-term cycling performance of g-CN-CNF-800 using longer discharge/charge time length (30 min/30 min).

Conflict of interest

The authors declare no competing financial interests.

Acknowledgments

This work was supported by IBS-R006-A2. Y.-H. C. acknowledges the financial support from the Basic Science Research Program (2016R1D1A3B03934752) through the National Research Foundation of Korea (NRF), which is funded by the Ministry of Education.

Appendix A. Supplementary data

Supplementary material related to this article can be found, in the online version, at doi:<https://doi.org/10.1016/j.apcatb.2018.05.073>.

References

- [1] M. Oezaslan, F. Hascché, P. Strasser, Pt-based core-shell catalyst architectures for oxygen fuel cell electrodes, *J. Phys. Chem. Lett.* 4 (2013) 3273–3291.
- [2] O.-H. Kim, Y.-H. Cho, T.-Y. Jeon, J.W. Kim, Y.-H. Cho, Y.-E. Sung, Realization of both high-performance and enhanced durability of fuel cells: Pt-exoskeleton structure electrocatalysts, *ACS Appl. Mater. Interfaces* 7 (2015) 14053–14063.
- [3] O.-H. Kim, Y.-H. Cho, D.Y. Chung, M.J. Kim, J.M. Yoo, J.E. Park, H. Choe, Y.-E. Sung, Facile and gram-scale synthesis of metal-free catalysts: toward realistic applications for fuel cells, *Sci. Rep.* 5 (2015) 8376.
- [4] X. Wu, K. Scott, A Li-doped Co_3O_4 oxygen evolution catalyst for non-precious metal alkaline anion exchange membrane water electrolyzers, *Int. J. Hydrogen Energy* 38 (2013) 3123–3129.
- [5] J. Chang, Q. Lv, G. Li, J. Ge, C. Liu, W. Xing, Core-shell structured $\text{Ni}_{12}\text{P}_5/\text{Ni}_3(\text{PO}_4)_2$ hollow spheres as difunctional and efficient electrocatalysts for overall water electrolysis, *Appl. Catal. B* 204 (2017) 486–496.
- [6] W. Niu, Z. Li, K. Marcus, L. Zhou, Y. Li, R. Ye, K. Liang, Y. Yang, Surface-modified porous carbon nitride composites as highly efficient electrocatalyst for Zn-air batteries, *Adv. Energy Mater.* (2017) 1701642.
- [7] C.-Y. Su, H. Cheng, W. Li, Z.-Q. Liu, N. Li, Z. Hou, F.-Q. Bai, H.-X. Zhang, T.-Y. Ma, Atomic modulation of FeCo-nitrogen-carbon bifunctional oxygen electrodes for rechargeable and flexible all-solid-state zinc-air battery, *Adv. Energy Mater.* 7 (2017) 1602420.
- [8] X. Wu, X. Han, X. Ma, W. Zhang, Y. Deng, C. Zhong, W. Hu, Morphology-controllable synthesis of Zn-Co-mixed sulfide nanostructures on carbon fiber paper toward efficient rechargeable zinc-air batteries and water electrolysis, *ACS Appl. Mater. Interfaces* 9 (2017) 12574–12583.
- [9] B.-S. Lee, S.H. Ahn, H.-Y. Park, I. Choi, S.J. Yoo, H.-J. Kim, D. Henkensmeier, J.Y. Kim, S. Park, S.W. Nam, K.-Y. Lee, J.H. Jang, Development of electrodeposited IrO_2 electrodes as anodes in polymer electrolyte membrane water electrolysis, *Appl. Catal. B* 179 (2015) 285–291.
- [10] M. Shao, Q. Chang, J.-P. Dodelet, R. Chenitz, Recent advances in electrocatalysts for oxygen reduction reaction, *Chem. Rev.* 116 (2016) 3594–3657.
- [11] N.-T. Suen, S.-F. Hung, Q. Quan, N. Zhang, Y.-J. Xu, H.M. Chen, Electrocatalysis for the oxygen evolution reaction: recent development and future perspectives, *Chem. Soc. Rev.* 46 (2017) 337–365.
- [12] J. Zhu, P. Xiao, H. Li, S.A.C. Carabineiro, Graphitic carbon nitride: synthesis, properties, and applications in catalysis, *ACS Appl. Mater. Interfaces* 6 (2014) 16449–16465.
- [13] A. Thomas, A. Fischer, F. Goettmann, M. Antonietti, J.-O. Müller, R. Schlögl, J.M. Carlsson, Graphitic carbon nitride materials: variation of structure and morphology and their use as metal-free catalysts, *J. Mater. Chem.* 18 (2008) 4893–4908.
- [14] K. Kwon, Y.J. Sa, J.Y. Cheon, S.H. Joo, Ordered mesoporous carbon nitrides with graphitic frameworks as metal-free, highly durable, methanol-tolerant oxygen reduction catalysts in an acidic medium, *Langmuir* 28 (2012) 991–996.
- [15] Y. Zheng, J. Liu, J. Liang, M. Jaroniec, S.Z. Qiao, Graphitic carbon nitride materials: controllable synthesis and applications in fuel cells and photocatalysis, *Energy Environ. Sci.* 5 (2012) 6717–6731.
- [16] T.Y. Ma, S. Dai, M. Jaroniec, S.Z. Qiao, Graphitic carbon nitride nanosheet-carbon nanotube three-dimensional porous composites as high-performance oxygen evolution electrocatalysts, *Angew. Chem. Int. Ed.* 53 (2014) 7281–7285.
- [17] J. Tian, Q. Liu, A.M. Asiri, K.A. Alamry, X. Sun, Ultrathin graphitic C_3N_4 nanosheets/graphene composites: efficient organic electrocatalyst for oxygen evolution reaction, *ChemSusChem* 7 (2014) 2125–2130.
- [18] X. Li, P. Cui, W. Zhong, J. Li, X. Wang, Z. Wang, J. Jiang, Graphitic carbon nitride supported single-atom catalysts for efficient oxygen evolution reaction, *Chem. Commun.* 52 (2016) 13233–13236.
- [19] N. Mansor, T.S. Miller, I. Dedigama, A.B. Jorge, J. Jia, V. Brázdová, C. Mattevi, C. Gibbs, D. Hodgson, P.R. Shearing, C.A. Howard, F. Corà, M. Shaffer, D.J.L. Brett, P.F. McMillan, Graphitic carbon nitride as a catalyst support in fuel cells and electrolyzers, *Electrochim. Acta* 222 (2016) 44–57.
- [20] W.-J. Ong, L.-L. Tan, Y.H. Ng, S.-T. Yong, S.-P. Chai, Graphitic carbon nitride ($\text{g-C}_3\text{N}_4$)-based photocatalysts for artificial photosynthesis and environmental remediation: are we a step closer to achieving sustainability? *Chem. Rev.* 116 (2016) 7159–7329.
- [21] Y. Zheng, Y. Jiao, Y. Zhu, Q. Cai, A. Vasileff, L.H. Li, Y. Han, Y. Chen, S.-Z. Qiao, Molecule-level $\text{g-C}_3\text{N}_4$ coordinated transition metals as a new class of electrocatalysts for oxygen electrode reactions, *J. Am. Chem. Soc.* 139 (2017) 3336–3339.
- [22] K. Qiu, Z.X. Guo, Hierarchically porous graphene sheets and graphitic carbon nitride intercalated composites for enhanced oxygen reduction reaction, *J. Mater. Chem. A* 2 (2014) 3209–3215.
- [23] I. Vincent, A. Kruger, D. Bessarabov, Development of efficient membrane electrode assembly for low cost hydrogen production by anion exchange membrane electrolysis, *Int. J. Hydrogen Energy* 42 (2017) 10752–10761.
- [24] X. Wu, K. Scott, A polymethacrylate-based quaternary ammonium OH^- ionomer binder for non-precious metal alkaline anion exchange membrane water electrolyzers, *J. Power Sources* 214 (2012) 124–129.
- [25] L. Xiao, S. Zhang, J. Pan, C. Yang, M. He, L. Zhuang, J. Lu, First implementation of alkaline polymer electrolyte water electrolysis working only with pure water, *Energy Environ. Sci.* 5 (2012) 7869–7871.
- [26] Z. Mingdao, D. Quanbin, Z. Hegen, C. Mindong, D. Liming, Novel MOF-Derived Co@N-C bifunctional catalysts for highly efficient Zn-Air batteries and water splitting, *Adv. Mater.* 30 (2018) 1705431.
- [27] Z. Pei, H. Li, Y. Huang, Q. Xue, Y. Huang, M. Zhu, Z. Wang, C. Zhi, Texturing in situ: N,S-enriched hierarchically porous carbon as a highly active reversible oxygen electrocatalyst, *Energy Environ. Sci.* 10 (2017) 742–749.
- [28] M.K. Cho, H.-Y. Park, S. Choe, S.J. Yoo, J.Y. Kim, H.-J. Kim, D. Henkensmeier, S.Y. Lee, Y.-E. Sung, H.S. Park, J.H. Jang, Factors in electrode fabrication for performance enhancement of anion exchange membrane water electrolysis, *J. Power Sources* 347 (2017) 283–290.
- [29] J. Fu, Z.P. Cano, M.G. Park, A. Yu, M. Fowler, Z. Chen, Electrically rechargeable zinc-air batteries: progress, challenges, and perspectives, *Adv. Mater.* 29 (2017) 1604685.
- [30] C.G. Liu, X.T. Wu, X.F. Li, X.G. Zhang, Synthesis of graphene-like $\text{g-C}_3\text{N}_4/\text{Fe}_3\text{O}_4$ nanocomposites with high photocatalytic activity and applications in drug delivery, *RSC Adv.* 4 (2014) 62492–62498.
- [31] X. She, L. Liu, H. Ji, Z. Mo, Y. Li, L. Huang, D. Du, H. Xu, H. Li, Template-free synthesis of 2D porous ultrathin nonmetal-doped $\text{g-C}_3\text{N}_4$ nanosheets with highly efficient photocatalytic H_2 evolution from water under visible light, *Appl. Catal. B* 187 (2016) 144–153.
- [32] J. Meng, Q. Lin, S. Wu, J. Pei, X. Wei, J. Li, Z. Zhang, Hybrid CN-MEA microplates with enhanced photocatalytic hydrogen evolution under visible light irradiation, *Catal. Sci. Technol.* 7 (2017) 3777–3784.
- [33] S. Hu, L. Ma, F. Li, Z. Fan, Q. Wang, J. Bai, X. Kang, G. Wu, Construction of $\text{g-C}_3\text{N}_4/\text{S-g-C}_3\text{N}_4$ metal-free isotype heterojunctions with an enhanced charge driving force and their photocatalytic performance under anoxic conditions, *RSC Adv.* 5 (2015) 90750–90756.
- [34] C. Hu, L. Dai, Multifunctional carbon-based metal-free electrocatalysts for simultaneous oxygen reduction, oxygen evolution, and hydrogen evolution, *Adv. Mater.* 29 (2017) 1604942.
- [35] S.M. Hafiz, R. Ritikos, T.J. Whitcher, N. Md, D.C.S. Razib, N. Bien, H. Chanlek, T. Nakajima, P. Saisopa, N.M. Songsiririthigul, S.A. Huang, Rahman, A practical carbon dioxide gas sensor using room-temperature hydrogen plasma reduced graphene oxide, *Sens. Actuators, B* 193 (2014) 692–700.
- [36] X. Li, Y. Fang, X. Lin, M. Tian, X. An, Y. Fu, R. Li, J. Jin, J. Ma, MOF derived Co_3O_4 nanoparticles embedded in N-doped mesoporous carbon layer/MWCNT hybrids: extraordinary bi-functional electrocatalysts for OER and ORR, *J. Mater. Chem. A* 3 (2015) 17392–17402.
- [37] X. Liu, W. Zhou, L. Yang, L. Li, Z. Zhang, Y. Ke, S. Chen, Nitrogen and sulfur doped porous carbon derived from human hair as highly efficient metal-free electrocatalysts for hydrogen evolution reactions, *J. Mater. Chem. A* 3 (2015) 8840–8846.
- [38] T. Sharifi, G. Hu, X. Jia, T. Wågberg, Formation of active sites for oxygen reduction reactions by transformation of nitrogen functionalities in nitrogen-doped carbon nanotubes, *ACS Nano* 6 (2012) 8904–8912.
- [39] T. Xing, Y. Zheng, L.H. Li, B.C.C. Cowie, D. Gunzelmann, S.Z. Qiao, S. Huang, Y. Chen, Observation of active sites for oxygen reduction reaction on nitrogen-doped multilayer graphene, *ACS Nano* 8 (2014) 6856–6862.
- [40] S.N. Faisal, E. Haque, N. Noorbehesht, W. Zhang, A.T. Harris, T.L. Church, A.I. Minett, Pyridinic and graphitic nitrogen-rich graphene for high-performance supercapacitors and metal-free bifunctional electrocatalysts for ORR and OER, *RSC Adv.* 7 (2017) 17950–17958.
- [41] Q. Wang, L. Shang, R. Shi, X. Zhang, Y. Zhao, G.I.N. Waterhouse, L.-Z. Wu, C.-H. Tung, T. Zhang, NiFe layered double hydroxide nanoparticles on Co,N-codoped carbon nanoframes as efficient bifunctional catalysts for rechargeable zinc-air batteries, *Adv. Energy Mater.* 7 (2017) 1700467.
- [42] J. Zhang, Z. Zhao, Z. Xia, L. Dai, A metal-free bifunctional electrocatalyst for oxygen reduction and oxygen evolution reactions, *Nat. Nanotechnol.* 10 (2015) 444–452.
- [43] B. Li, S.-W. Chien, X. Ge, J. Chai, X.-Y. Goh, K.-T. Nai, T.S. Andy Hor, Z. Liu, Y. Zong, Ni/NiOx-decorated carbon nanofibers with enhanced oxygen evolution activity for rechargeable zinc-air batteries, *Mater. Chem. Front.* 1 (2017) 677–682.
- [44] J.S. Yi, T.-w. Song, Performance characterization of PEM fuel cells using AC impedance spectroscopy: I. Model-based analysis, *J. Electrochem. Soc.* 160 (2012) F141–F152.
- [45] Y.-C. Cao, X. Wu, K. Scott, A quaternary ammonium grafted poly vinyl benzyl chloride membrane for alkaline anion exchange membrane water electrolyzers with no-noble-metal catalysts, *Int. J. Hydrogen Energy* 37 (2012) 9524–9528.